Journal of Theoretical Biology 356 (2014) 71–84

Contents lists available at ScienceDirect

Journal of Theoretical Biology

journal homepage: www.elsevier.com/locate/yjtbi

Are *in vitro* estimates of cell diffusivity and cell proliferation rate sensitive to assay geometry?

Katrina K. Treloar [a,b], Matthew J. Simpson [a,b,*], D.L. Sean McElwain [b], Ruth E. Baker [c]

[a] Mathematical Sciences, Queensland University of Technology (QUT), Brisbane, Australia
[b] Tissue Repair and Regeneration Program, Institute of Health and Biomedical Innovation, QUT, Brisbane, Australia
[c] Wolfson Centre for Mathematical Biology, Mathematical Institute, University of Oxford, United Kingdom

HIGHLIGHTS

- Spread of cell populations in two distinct *in vitro* assay geometries is analysed.
- Discrete and continuum models are compared to experimental results.
- Geometry of *in vitro* assay affects estimates of cell diffusivity by up to 50%.
- Cell proliferation rate estimates vary by up to 30% depending on assay geometry.
- Parameterised models accurately predict behaviour of spreading cell populations.

ARTICLE INFO

Article history:
Received 28 November 2013
Received in revised form
6 March 2014
Accepted 18 April 2014
Available online 28 April 2014

Keywords:
Circular barrier assay
Cancer
Wound-healing
Collective cell spreading
Random walk model

ABSTRACT

Cells respond to various biochemical and physical cues during wound-healing and tumour progression. *in vitro* assays used to study these processes are typically conducted in one particular geometry and it is unclear how the assay geometry affects the capacity of cell populations to spread, or whether the relevant mechanisms, such as cell motility and cell proliferation, are somehow sensitive to the geometry of the assay. In this work we use a circular barrier assay to characterise the spreading of cell populations in two different geometries. Assay 1 describes a tumour-like geometry where a cell population spreads outwards into an open space. Assay 2 describes a wound-like geometry where a cell population spreads inwards to close a void. We use a combination of discrete and continuum mathematical models and automated image processing methods to obtain independent estimates of the effective cell diffusivity, D, and the effective cell proliferation rate, λ. Using our parameterised mathematical model we confirm that our estimates of D and λ accurately predict the time-evolution of the location of the leading edge and the cell density profiles for both assay 1 and assay 2. Our work suggests that the effective cell diffusivity is up to 50% lower for assay 2 compared to assay 1, whereas the effective cell proliferation rate is up to 30% lower for assay 2 compared to assay 1.

1. Introduction

Cell migration and cell proliferation are essential mechanisms that drive wound-healing and tumour progression (Clark, 1996; Geho et al., 2005; Martin, 1997; Weinberg, 2006; Woodhouse et al., 1997). During these processes, cells sense and respond to various biochemical and physical cues (Ashby and Zijlstra, 2012; Brock et al., 2003; Kilian et al., 2010; Lutolf and Hubbell, 2005; Vogel and Sheetz, 2006). Although the role of biochemical cues has been widely explored, it remains relatively unclear how physical cues, such as the local geometry, affect the capacity of cell populations to spread (Ashby and Zijlstra, 2012; Brock et al., 2003; Kilian et al., 2010; Lutolf and Hubbell, 2005; Vogel and Sheetz, 2006).

Wound-healing and tumour progression are often studied in the same context since the mechanisms that drive these processes are thought to be similar (Weinberg, 2006; Coussens and Werb, 2002; Chang et al., 2004; Friedl and Gilmour, 2009; Schafer and Werner, 2008). Despite their similarities, these processes have distinct geometries: (i) during wound-healing, cell populations spread inwards to close the wound void, and (ii) during tumour

* Corresponding author at: Mathematical Sciences, Queensland University of Technology (QUT), Brisbane, Australia. Tel.: +617 3138 5241; fax: +617 3138 2310.
E-mail address: matthew.simpson@qut.edu.au (M.J. Simpson).

http://dx.doi.org/10.1016/j.jtbi.2014.04.026

progression, cell populations spread outwards causing the tumour to expand (Weinberg, 2006; Ashby and Zijlstra, 2012).

Cell-based assays are commonly used to quantify the capacity of cell populations to spread *in vitro* (Ashby and Zijlstra, 2012; Kramer et al., 2013; Decaestecker et al., 2007; Kam et al., 2008, 2009; Valster et al., 2005). Several types of assays have been developed to investigate cell population spreading in two and three dimensions including Transwell, scratch, exclusion zone and spheroid assays (Ashby and Zijlstra, 2012; Kramer et al., 2013; Decaestecker et al., 2007; Valster et al., 2005). While these assays have been used to study the behaviour of various cell lines *in vitro*, most studies neglect to explicitly consider the role of geometry when conducting or interpreting these assays and it is unclear how results obtained for one particular geometry translate into another (Ashby and Zijlstra, 2012; Kramer et al., 2013; Decaestecker et al., 2007; Valster et al., 2005). Recent work using microfabrication methods focused on creating various-sized channels through which cells could migrate, with the observation that the speed of the leading edge of the cell population depends on the channel width (Vedula et al., 2012). Therefore, it seems reasonable to assume that assay geometry could play a role in determining the rate at which cell populations spread.

An alternative approach to understand how differences in geometry affect cell population spreading is to conduct a two-dimensional cell spreading assay where the direction of the spreading is intentionally varied. In this work, we will consider two types of assays:

Assay 1: This is a tumour-like assay initialised by placing cells inside a barrier, which is then lifted, allowing the population to spread outwards (Ashby and Zijlstra, 2012; Kramer et al., 2013).

Assay 2: This is a wound-like assay initiated by placing cells outside a barrier, which is then lifted, allowing the population to spread inwards (Ashby and Zijlstra, 2012; Kramer et al., 2013).

Without analysing any experimental data it is unclear whether a population of otherwise identical cells will exhibit different rates of spreading in the geometry of assay 1 compared to the geometry of assay 2.

A circular barrier assay can be used to study both assay 1 and assay 2 geometries, by initially placing the cells either inside or outside the barrier, which is then lifted to initiate the cell spreading (Ashby and Zijlstra, 2012; Kramer et al., 2013; Simpson et al., 2013; Treloar and Simpson, 2013; Van Horssen and Ten Hagen, 2010). Barrier assays are thought to be more reproducible than traditional mechanical wounding assays, such as scratch assays, as they do not damage the cell monolayer (Van Horssen and Ten Hagen, 2010; Gough et al., 2011). In this work, we will consider the spreading of cell populations in a barrier assay that are driven by combinations of motility and proliferation.

The standard continuum mathematical model used to describe how a population of motile and proliferative cells spread in two dimensions is related to the Fisher–Kolmogorov equation, and is given by

$$\frac{\partial \overline{c}}{\partial t} = D\nabla^2\overline{c} + \lambda\overline{c}\left(1-\frac{\overline{c}}{K}\right), \tag{1}$$

where $\overline{c}(x,y,t)$ [cells/L^2] is the dimensional cell density, D [L^2/T] is the cell diffusivity (random motility coefficient), λ [/T] is the cell proliferation rate and K [cells/L^2] is the carrying-capacity density (Murray, 2002; Sherratt and Murray, 1990; Swanson et al., 2003; Maini et al. 2004a,b; Sengers et al., 2007; Cai et al., 2007). Physical dimensions relevant to *in vitro* cell biology assays are μm and hours for L and T, respectively. Discrete random walk-based models which are related to Eq. (1) can also be used to study cell population spreading. Discrete models allow us to visualise the biological spreading process in a way that is directly comparable with experimental results (Simpson et al., 2013; Anderson et al., 2007; Anderson and Chaplain, 1998; Aubert et al., 2006; Deroulers et al., 2009; Codling et al., 2008; Simpson et al., 2010; Turner and Sherratt, 2002; Turner et al., 2004; McDougall et al., 2012). For example, snapshots from a discrete model showing the location of individual agents in the population can be easily compared to experimental images that show the location of individual cells in the population (Simpson et al., 2013; Treloar et al., 2013).

Previous studies have used Eq. (1) to estimate D and λ from experimental observations with the additional implicit assumption that these estimates could be relevant when considering the same cell population spreading in a different geometry. This standard assumption implies that estimates of D and λ obtained by calibrating Eq. (1) to observations in one particular geometry could be used to accurately predict the spreading of the same cell population, under the same experimental conditions, in a different geometry. However, from a biological point of view, it seems reasonable to anticipate that cell populations could respond differently under different circumstances. This means that our estimates of D and λ in Eq. (1) might be different when calibrating this model to different experimental conditions. For this reason we will refer to estimates of D as the *effective cell diffusivity* and our estimates of λ as the *effective cell proliferation rate*, thereby making it explicit that we are allowing for the possibility that these estimates could depend on the specific details for the experiment from which they are estimated.

In this work, we use a combined experimental and mathematical modelling approach to investigate how the two-dimensional spreading of a fibroblast cell population is influenced by the assay geometry. In particular, we address the following questions:

1. Do estimates of the effective cell diffusivity, D, depend on the geometry of the assay?
2. Do estimates of the effective cell proliferation rate, λ, depend on the geometry of the assay?
3. Does the geometry of the assay affect the rate at which the leading edge of the cell population moves?
4. Are the cell density profiles through the spreading cell population sensitive to changes in the geometry of the assay?

To answer these questions, we conduct several circular barrier experiments using assay 1 and assay 2 geometries. For both assay geometries we independently estimate the effective cell diffusivity, D, using experiments where cell proliferation is suppressed. The effective proliferation rate, λ, is then separately estimated using experiments where proliferation is not suppressed. To ensure that our estimates of D and λ accurately predict the position of the leading edge of the spreading population as well as the cell density profile throughout the spreading cell population we compare predictions of the parameterised mathematical model with experimental measurements. In summary, our results indicate that estimates of D and λ appear to depend on the assay geometry, with D being more sensitive than λ.

2. Experimental methods

2.1. Circular barrier assay

Fig. 1 shows a schematic diagram of the two barrier assay geometries considered in this work. To perform these assays metal-silicone barriers (Aix Scientifics, Germany) were cleaned, sterilised, dried and placed in the centre of the wells of a 24-well tissue culture plate. The wells in the tissue culture plate have a diameter of 15,600 μm. The barrier has an approximate radius of 3000 μm inside the silicone tip (located at the end of the barrier) and 4000 μm outside the silicone tip.

Experiments were conducted with fibroblast cells (supplementary material) where, in some cases the spreading was driven by

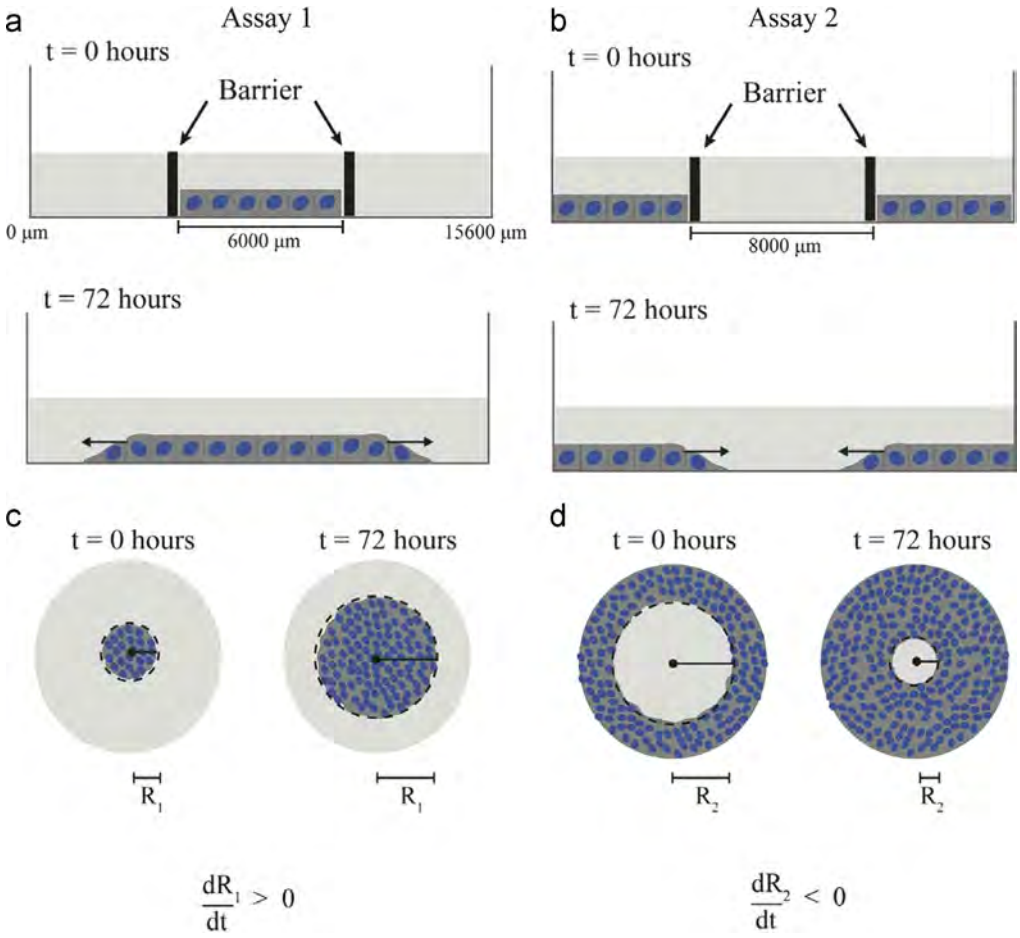

Fig. 1. Schematic of the circular barrier assay for assay 1 and assay 2 (not to scale). (a) Assay 1: cells are placed inside the barrier allowing the cell population to spread outwards. (b) Assay 2: cells are placed outside the barrier allowing the cell population to spread inwards. The population-scale views for the assay 1 and assay 2 geometries are shown in (c) and (d), respectively, and indicate the radii measurements that were extracted from assay 1 and assay 2. Here, R_1 corresponds to the radius of the circular area enclosed by the spreading cell population for assay 1 ($dR_1/dt > 0$) and R_2 indicates the radius of the circular void area for assay 2 ($dR_2/dt < 0$).

cell motility only, whereas in other cases the spreading was driven by a combination of cell motility and cell proliferation. For those experiments where cell proliferation was suppressed, Mitomycin-C (Sigma Aldrich, Australia) was added to the cell solutions for one hour before the assays were initialised (Sadeghi et al., 1998). Experiments using assay 1 and assay 2 geometries were initialised by carefully placing the cells either inside (Fig. 1 (a)) or outside (Fig. 1(b)) the barrier, respectively. In all cases great care was taken to ensure that the cells were approximately evenly distributed at the beginning of the experiment. All experiments were repeated using two different initial cell densities: low density (3.5×10^{-4} cells/μm^2) and high density (1.1×10^{-3} cells/μm^2). After initially placing the cells in or around the barrier, the tissue culture plate was left for one hour in a humidified incubator at 37 °C and 5% CO_2 to allow the cells to attach to the surface, after which the barriers were removed and the cell layer was washed with serum free medium (SFM; culture medium without FCS) and replaced with 0.5 mL of culture medium. Plates were incubated at 37 °C in 5% CO_2 for four different durations, $t=0$, 24, 48 and 72 h. Each assay, for each time point, for each initial density and for each geometry, was repeated in triplicate ($n=3$).

2.2. Image acquisition and analysis

Two types of images were acquired from each experiment: (i) population-scale images showing the location of the entire spreading population, and (ii) individual-scale images detailing the location of individual cells within the spreading population. Details of the image acquisition and analysis are given in the Supplementary material.

Schematic population-scale images of assay 1 and assay 2 are shown in Fig. 1 (c) and (d), respectively. We use a standard approach to measure the observed spreading by estimating the radius, R, from the centre of the well to the leading edge of the cell population as shown in Fig. 1 (c) and (d). Here, R_1 corresponds to the radius of the spreading cell population in assay 1, and R_2 represents the radius of the void space in assay 2. Estimates of R_1 and R_2 were obtained by locating the position of the leading edge of the spreading cell populations using customised image processing software that was written using the MATLAB image processing toolbox (v7.12) (MATLAB, 2014) (Supplementary material). The same image analysis methods used to detect the location of the experimental leading edge were applied to detect the edges in the snapshots produced by the discrete model described in Section 3. For assay 1, the area (*regionprops*) of the spreading population, A, was estimated and converted into an equivalent circular radius, $R_1 = \sqrt{A/\pi}$. For assay 2, the area of the void region, A, was estimated and converted into an equivalent circular radius, $R_2 = \sqrt{A/\pi}$.

Individual-scale images were used to construct a detailed transect across the spreading populations. Overlapping images were acquired at regular spatial intervals from the leading edge of the cell population to either the centre of the well (assay 1) or the edge of the well (assay 2). Automated image analysis,

supplemented with manual counting, was used to count the number of individual cells within various subregions across the transects and these counts were used to construct detailed cell density profiles (Supplementary material).

3. Modelling methods

To quantify and interpret our experimental observations, we use an interacting random walk model which is related to Eq. (1). The details of our discrete model have been previously reported in Simpson et al. (2010).

3.1. Discrete model

The discrete model is implemented on a two-dimensional square lattice with spacing Δ, which corresponds to the average diameter of the cells. We estimate Δ by measuring the area of several cells using ImageJ (2013) software and convert these estimates into an equivalent circular diameter, giving $\Delta \approx 25$ μm. We assume that the cells form a two-dimensional monolayer, which is reasonable since our images indicate that individual cells do not pile up onto other cells in the vertical direction. To account for volume exclusion and finite size effects, the model permits only one agent to occupy each lattice site (Deroulers et al., 2009; Simpson et al., 2010). This exclusion mechanism explicitly accounts for any differences in the availability of free space in assay 1 compared to assay 2. Each site is indexed (i,j), where i, $j \in \mathbb{Z}^+$, and each site has position $(x,y)=(i\Delta, j\Delta)$. Simulations are initialised by placing agents uniformly, at random, either inside a circle of radius 3000 μm located at the centre of the lattice for assay 1 simulations, or outside a circle of radius 4000 μm for assay 2 simulations. Here, the initial radii for assay 1 and assay 2 correspond to the physical internal and external radii imposed by the silicone tip of the barrier.

A random sequential update method (Chowdhury et al., 2005) is used to perform the simulations. If there are $N(t)$ agents at time t, during the next time step of duration τ, $N(t)$ agents are selected at random, one at a time, and given the opportunity to move with probability $P_m \in [0,1]$. We use an unbiased motility mechanism where an agent at (x,y) attempts to step to $(x\pm\Delta, y)$ or $(x, y\pm\Delta)$ with equal probability of 1/4. Once the $N(t)$ potential motility events have been assessed, another $N(t)$ agents are selected at random, one at a time, and given the opportunity to proliferate with probability $P_p \in [0,1]$. We model proliferation with an unbiased mechanism whereby a proliferative agent at (x,y) attempts to deposit a daughter agent at $(x\pm\Delta, y)$ or $(x, y\pm\Delta)$, with each target site chosen with equal probability of 1/4. Potential motility and proliferation events that would place an agent on an occupied site are aborted (Deroulers et al., 2009; Simpson et al., 2010).

3.2. Continuum model

To relate the discrete model to Eq. (1), we note that the average occupancy of site (i,j), evaluated using $\mathcal{R}$ identically prepared realisations, is

$$\langle C_{i,j}\rangle = \frac{1}{\mathcal{R}}\sum_{k=1}^{\mathcal{R}} C_{i,j}^k, \tag{2}$$

here the superscript denotes the kth identically prepared realisation of the same stochastic process and the occupancy of site (i,j) is denoted by $C_{i,j}^k$, with $C_{i,j}^k=1$ for an occupied site, and $C_{i,j}^k=0$ for a vacant site. The corresponding continuous density, $\overline{c}(x,y,t)$, is governed by Eq. (1) with carrying capacity, $K=1$ agents/lattice site (Simpson et al., 2010).

The associated diffusivity and proliferation rate (Simpson et al., 2010) are given by

$$D=\frac{P_m}{4}\lim_{\Delta,\tau\to 0}\left(\frac{\Delta^2}{\tau}\right), \quad \lambda=\lim_{\tau\to 0}\left(\frac{P_p}{\tau}\right). \tag{3}$$

We note that $\langle C_{i,j}\rangle \in [0,1]$ is equivalent to $\overline{c}(x,y,t)$ as $\mathcal{R}\to\infty$, provided that P_p/P_m is sufficiently small (Simpson et al., 2010). Strictly speaking, the continuum model is valid in the limit that $\Delta\to 0$ and $\tau\to 0$ jointly with the ratio Δ^2/τ held constant, implying that $P_p=\mathcal{O}(\tau)$ (Simpson et al., 2010). As we will show in Section 4, the cell populations in all assays maintain an approximately circular geometry for the entire duration of the experiment (Section 4.1), hence, we implement Eq. (1) in an axisymmetric coordinate system

$$\frac{\partial c}{\partial t}=D\left(\frac{\partial^2 c}{\partial r^2}+\frac{1}{r}\frac{\partial c}{\partial r}\right)+\lambda c(1-c), \tag{4}$$

where the dimensional cell density, $\overline{c}(r,t)$, has been scaled relative to the carrying capacity density, $c(r,t)=\overline{c}(r,t)/K$ so that $c(r,t)\in[0,1]$. We estimate the carrying capacity density by making the standard assumption that the maximum packing density of cells corresponds to a square packing (Simpson et al., 2013). Since $\Delta\approx 25$ μm, we have $K=1/25^2\approx 1.6\times 10^{-3}$ cells/μm^2 (Simpson et al., 2013).

Numerical solutions of Eq. (4) are obtained using a finite-difference approximation on a grid with a uniform grid spacing δr, and implicit Euler stepping with uniform time steps of duration δt (Bradie, 2005; Simpson et al., 2005). Picard iteration, with absolute convergence tolerance, ϵ, is used to solve the resulting system of nonlinear equations. For all numerical results presented we tested that the numerical solutions were grid independent. Solutions of Eq. (4) are obtained on the domain $0\le r\le 7800$ μm, with a symmetry condition, $\partial c/\partial r=0$, at $r=0$ μm and a zero flux boundary condition at $r=7800$ μm for both assay 1 and assay 2 geometries. The value $r=7800$ μm corresponds to the physical radius of the well ($r=15,600/2$). The initial condition for assay 1 is given by

$$c(r,0)=\begin{cases} c_0, & 0\le r\le 3000\ \mu\text{m},\\ 0, & 3000\le r\le 7800\ \mu\text{m}, \end{cases} \tag{5}$$

where $c_0\in[0,1]$ is the initial nondimensional cell density within the barrier. The initial condition for assay 2 is given by

$$c(r,0)=\begin{cases} 0, & 0\le r< 4000\ \mu\text{m},\\ c_0, & 4000\le r\le 7800\ \mu\text{m}. \end{cases} \tag{6}$$

The initial nondimensional cell density for low density experiments is $c_0=3.5\times 10^{-4}/1.6\times 10^{-3}\approx 0.22$, whereas the initial nondimensional cell density for the high density experiments is $c_0=1.1\times 10^{-3}/1.6\times 10^{-3}\approx 0.66$.

3.3. Standard measure of spatial spreading

In addition to analysing the data using the mathematical modelling framework described in Sections 3.1 and 3.2, we also interpret our results using a standard measure that is often reported in the experimental cell biology literature (Ashby and Zijlstra, 2012; Gough et al., 2011; Van Horssen and Ten Hagen, 2010; McKenzie et al., 2011; Treloar and Simpson, 2013; Zaritsky et al., 2011, 2013). This standard measure can be written as

$$M(t)=\frac{R_a(t)-R_a(0)}{R_a(0)}\times 100, \tag{7}$$

where $M(t)$ represents the percentage change in the observed radius at time t relative to the initial radius, $a=1$ or 2 represents

assay 1 and assay 2, respectively, and $R(t)$ is the detected radius at time t.

4. Results

4.1. Cell diffusivity estimates

We first investigated whether estimates of D were sensitive to the assay geometry. To identify D we considered experiments where cells were pretreated with Mitomycin-C to suppress cell proliferation. Population-scale images in Fig. 2(a) and (b) illustrate the distribution of cells in the assay 1 geometry at $t=0$ and $t=72$ h for an experiment with a high initial cell density inside the barrier. The corresponding images for the assay 2 geometry are shown in Fig. 2(c) and (d). For both geometries, the area occupied by the cell population increases with time and the circular geometry is maintained. From these images alone it is difficult to interpret whether the spreading in assay 1 is any different from the spreading in assay 2.

To quantify any differences between the observed spreading in assay 1 and assay 2, we used the image analysis methods (Section 2.2) to detect the position of the leading edge of the spreading cell populations in each geometry. The detected leading edges are superimposed onto the images in Fig. 2(a)–(d). For assay 1, the area enclosed by the leading edge was converted into an equivalent circular radius, R_1. Similarly, for assay 2, the area of the void space enclosed by the leading edge was converted into an equivalent circular radius, R_2. For the assay 1 population-scale images in Fig. 2, R_1 increases from 3000 μm to 4171 μm, over $t=72$ h, giving $M(72)=39\%$ using Eq. (7). Similarly, for the population-scale images of assay 2, R_2 decreases from 4000 μm to 2950 μm, giving $M(72)=-26\%$. The corresponding results for the experiments initialised with low cell density give $M(72)=26\%$ for assay 1 and $M(72)=-14\%$ for assay 2 (Supplementary material). Although it is straightforward to compute and compare estimates of $M(t)$ for the different assays, these estimates do not provide us with any quantitative insight into the role of the mechanisms that drive the spreading process.

We estimated D for each geometry by comparing the experimental data with simulation data from the discrete mathematical model. Simulations, as described in Section 3, were performed using the discrete model to replicate the initial distribution of cells in both geometries at both initial densities. To estimate D we performed simulations where we systematically varied the duration of the time step, τ, which is equivalent to varying the effective cell diffusivity, $D=P_m\Delta^2/(4\tau)$, in the continuum model. This procedure enabled us to determine the value of D that produces a prediction that best matches the experimental data. In all cases, we set $P_p=0$ and $P_m=1$. We considered 30 equally spaced values of D in the interval $D\in[0,5000]$ μm^2/h, and for each value of D we simulated each experiment three times ($n=3$), over $t=24$, 48 and 72 h. The image analysis software was used to the locate the position of the leading edge of the simulated cell populations in the same way that the image analysis was used to detect the leading edge in the experimental images. In all cases, the detected leading edge was converted to an equivalent circular radius.

Population-scale images in Fig. 2(f) and (g) show the distribution of agents in the discrete model in assay 1 and the corresponding

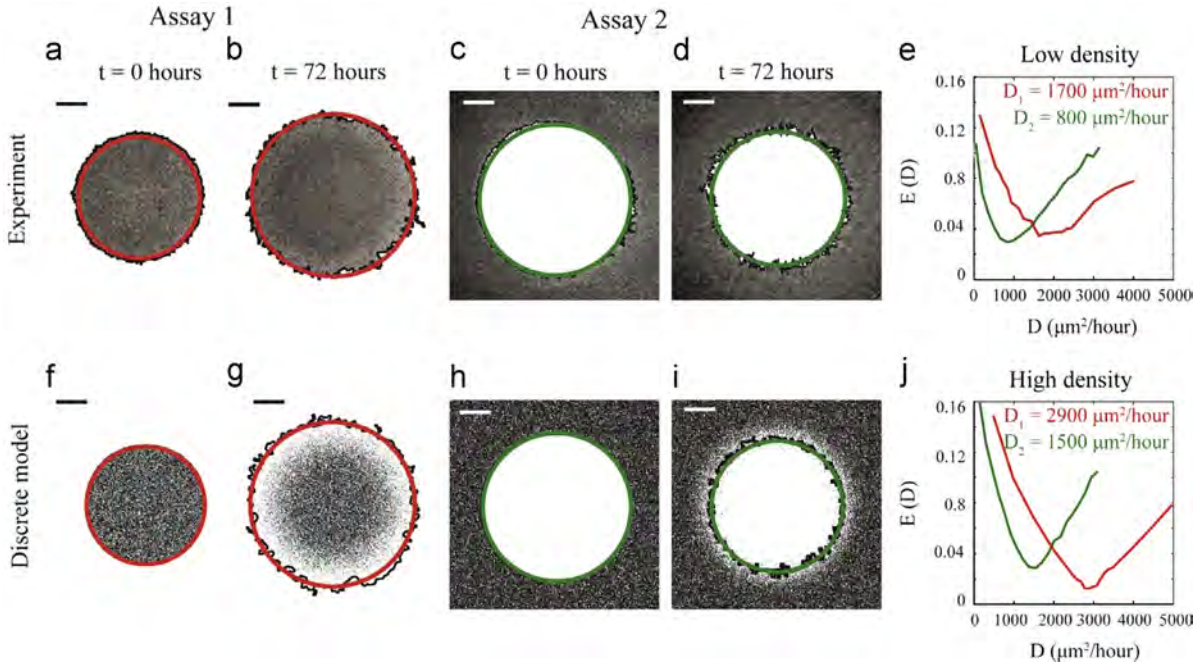

Fig. 2. Estimates of cell diffusivity. Experimental and modelling images are shown in (a)–(d) and (f)–(i) comparing the position of the leading edge of the spreading cell population for assay 1 and assay 2 geometries at high initial cell density. Experimental images in (a) and (b) show the distribution of cells at $t=0$ and $t=72$ h respectively for a barrier assay using the assay 1 geometry where cells are initially placed uniformly inside the barrier after Mitomycin-C pretreatment. Equivalent images using the assay 2 geometry, where cells are initially placed outside the barrier, are shown in (c) and (d). The black solid line indicates the position of the leading edge of the spreading population as detected by the image analysis software. The area enclosed by the spreading cell population was converted to an equivalent circular area. For the assay 1 geometry, the area detected encloses the spreading cell population, while for the assay 2 geometry, the area detected encloses the void. Images in (f)–(i) show the corresponding snapshots of the discrete model on a 624×624 lattice with $\Delta=25$ μm. Simulations were performed using $P_m=1$ and $P_p=0$. Model simulations in (f) and (g) correspond to $\tau=0.0526$ h and (h) and (i) correspond to $\tau=0.1000$ h. The detected leading edge of the discrete cell population is indicated by the black solid line. The red (assay 1) and green (assay 2) circles which are superimposed onto the experimental and discrete images correspond to the $c(r,t)=0.019$ contour of the numerical solution of Eq. (4) with $\lambda=0$, $D_1=2900$ μm^2/h and $D_2=1500$ μm^2/h. Results in (e) and (j) compare $E(D)$, using Eq. (8), between the position of the leading edge of the simulated cell population, using various values of D, and the position of the leading edge of the corresponding experimental image for assay 1 (red) and assay 2 (green) at low and high initial cell densities, respectively. The scale bar corresponds to 1500 μm. (For interpretation of the references to colour in this figure caption, the reader is referred to the web version of this paper.).

detected position of the leading edge, at $t=0$ and $t=72$ h, for an experiment where a high density cell population was initially placed inside the barrier. The population-scale images in Fig. 2 (h) and (i) illustrate the equivalent results for assay 2. We note that the distribution of agents in Fig. 2(g) and (i) does not appear to be influenced by the underlying lattice structure at this scale since the simulations were initialised at a relatively low density, and the density of agents at the leading edge is, by definition, very low. This qualitative observation is consistent with recent theoretical comparisons between lattice-based and lattice-free descriptions of spreading cell populations which confirmed that there is no difference between a lattice-based and a lattice-free model at the leading edge of spreading populations (Plank and Simpson, 2013).

To determine the value of D for which our model results best match the observed data, we compared the radii estimates from the discrete simulations, at $t=24$, 48 and 72 h, to the corresponding experimental data, using an estimate of the least-squares error given by

$$E(D)=\frac{\sum_{i=1}^{3}(ER_a^i-SR_a^i)^2}{\sum_{i=1}^{3}(ER_a^i)^2}, \tag{8}$$

where i indicates the three time points, $t=24$, 48 and 72 hours, and a corresponds to the assay geometries, 1 and 2. In all cases, ER and SR are the radii extracted from the experimental cell populations and the corresponding simulated populations, respectively, averaged over ($n=3$) identically prepared replicates.

Results in Fig. 2(e) and (j) show $E(D)$ for experiments in each geometry for both initial cell densities. For all experiments there is a well-defined minimum which indicates the least-squares estimate of D. We note that the estimate of D is different for each geometry and each initial cell density. Our analysis indicates that for experiments using a low initial cell density we have $D\approx 1700\ \mu m^2/h$ for assay 1, while $D\approx 800\ \mu m^2/h$ for assay 2. Our results for the experiments using a high initial cell density show a similar trend where $D\approx 2900\ \mu m^2/h$ for assay 1, while $D\approx 1500\ \mu m^2/h$ for assay 2. For both initial cell densities, our least-squares estimate of D is approximately 50% smaller for assay 2. These differences suggest that the cell motility mechanism is affected by the assay geometry and we note that these differences were not obvious through visual inspection of the experimental images or through the use of the commonly reported quantity, $M(t)$, given by Eq. (7).

To confirm that our estimates of D allow us to accurately model the experimental data we compared the numerical solution of Eq. (4), with $\lambda=0$, to population-scale images from the experiments and discrete simulations in Fig. 2(a)–(d) and (f)–(i). To compare the numerical solution of Eq. (4) with the experimental images we choose an appropriate contour of the solution, $c(r,t)=0.019$, which best describes the averaged spreading observed in the experiments (Supplementary material). The correspondence between the position of the leading edge in the experimental images and the $c(r,t)=0.019$ contour of the solution of Eq. (4) in Fig. 2(a)–(d) and (f)–(i) confirms that our estimates of D are appropriate for each geometry and initial cell density.

4.2. Cell proliferation estimates

To estimate λ we considered experiments where proliferation was not suppressed. Individual-scale images were used together with the image analysis techniques to count the number of cells, at a fixed position, as a function of time. For each experiment, the number of cells in four different subregions, each of dimension 250 μm × 250 μm, was counted. The locations of the subregions were chosen so that the cell density at that location is approximately spatially uniform and locally we have $\overline{c}(r,t)\approx\overline{c}(t)$. The cell counts were converted into a measurement of the nondimensional cell density, $c(t)=\overline{c}(t)/K$. Fig. 3(a) and (f) illustrates the approximate location and

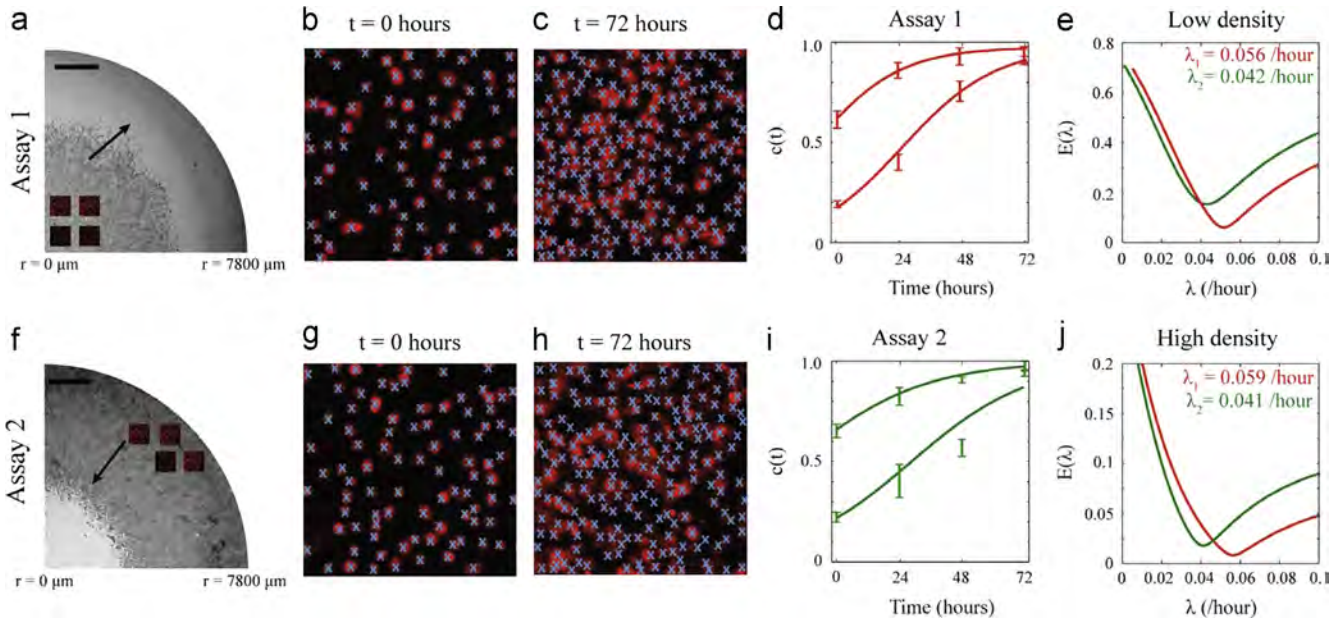

Fig. 3. Estimates of the cell proliferation rate. Cell proliferation rate estimates were obtained by counting the number of cells in four different subregions in each experimental replicate. The location of subregions was located away from the leading edge so that the cell density in that subregion was approximately spatially uniform giving $c(r,t)=c(t)$. The location and the size of the four subregions for assay 1 and assay 2 geometries are shown in (a) and (f) respectively, where the scale bar corresponds to 1500 μm. Images in (b) and (c) and (g) and (h) show snapshots of dimensions 250 μm × 250 μm for experiments with high cell density without Mitomycin-C pretreatment, at $t=0$ and $t=72$ h for assay 1 and assay 2 geometries, respectively. The Propidium Iodide staining highlights the cell nucleus and blue crosses indicate cells that were counted. Results in (d) and (i) compare the mean non-dimensional cell density ($n=4$) from experiments with an initial low and high cell density for both assay 1 (red) and assay 2 (green) at $t=0$, 24, 48 and 72 hours, with error bars indicating one standard deviation from the mean. The appropriately parameterised logistic growth curves using the cell proliferation rate estimates from Table 1 are superimposed in (d) and (i). Results in (e) and (j) show $E(\lambda)$, given by Eq. (11), for various values of λ, for experiments at low and high cell densities, respectively. (For interpretation of the references to colour in this figure caption, the reader is referred to the web version of this paper.)

size of each of the four subregions for assay 1 and assay 2, respectively.

Images in Fig. 3(b) and (c), and (g) and (h) show snapshots of a subregion analysed for assay 1 and assay 2, respectively. These results correspond to experiments that were initialised with a high cell density. We note that the cell density increases rapidly with time and that there appears to be no visual difference in the cell density behaviour between either geometry. The evolution of $c(t)$ is shown in Fig. 3(d) and (i) for both geometries and each initial cell density.

We note that Eq. (4) can be simplified when the cell density, $c(r,t)$, is spatially uniform so that locally we have $c(r,t)=c(t)$. Hence, Eq. (4) simplifies to the logistic equation

$$\frac{dc(t)}{dt}=\lambda c(t)(1-c(t)), \tag{9}$$

which has the solution

$$c(t)=\frac{c(0)\exp(\lambda t)}{1+c(0)(\exp(\lambda t)-1)}, \tag{10}$$

where $c(0)$ is the nondimensional initial cell density.

To estimate λ, we found the value of λ that minimised an estimate of the least-squares error between our experimental measurements and Eq. (10), given by

$$E(\lambda)=\frac{\sum_{i=1}^{3}(EP_a^i-SP_a^i)^2}{\sum_{i=1}^{3}(EP_a^i)^2}, \tag{11}$$

where i denotes the three time points, $t=24$, 48 and 72 h, and a corresponds to the assay geometries, 1 and 2. In all cases, EP corresponds to the nondimensional cell density extracted from the experimental images averaged over ($n=4$) replicates and SP is the corresponding nondimensional cell density using Eq. (10).

Results in Fig. 3(e) and (j) show $E(\lambda)$ for experiments in both geometries and both initial cell densities. For all cases, our results show that there is a well-defined minimum in $E(\lambda)$. For experiments without Mitomycin-C pretreatment at low density we have $\lambda=0.056$/h for assay 1 and $\lambda=0.042$/h for assay 2. Similarly, for the experiments without Mitomycin-C pretreatment at high density we have $\lambda=0.059$/h for assay 1 and $\lambda=0.041$/h for assay 2. The relevant logistic growth curves, given by Eq. (10) with our estimates of λ, are superimposed in Fig. 3(d) and (i). These growth curves confirm that, on average, our estimates of λ provide a good match to the observed data.

To explore whether our estimates of λ are sensitive to the location of the subregion, we re-estimated λ in two additional subregions located in different positions that were at least 2000 μm behind the leading edge (Supplementary material). These additional results show that there is a relatively small variation in λ, confirming that our estimates of λ are relatively insensitive to the choice of the location of the subregions, provided that we are sufficiently far behind the leading edge where $\bar{c}(r,t)\approx\bar{c}(t)$. Therefore, given this insensitivity, we will use the values of λ reported here in the main manuscript. We also estimated λ for the experiments with Mitomycin-C pretreatment (Supplementary material) where cell proliferation was assumed to be suppressed. This gave $\lambda<0.003$/h, indicating that the number of cells did not significantly increase or decrease over the duration of the experiment. This implies that Mitomycin-C pretreatment prevented proliferation and did not induce cell death.

4.3. Predicting the behaviour of spreading cell populations in different geometries

A summary of our estimates of D and λ for both geometries and both initial cell densities is given in Table 1. The variability in our estimates is also reported, and the details of how the variability was determined are given in the Supplementary material.

We will now consider whether the parameterised mathematical model can accurately predict the position of the leading edge of the spreading cell populations and the details of the cell density profiles throughout the entire spreading cell populations.

4.3.1. Position of the leading edge

Population-scale images in Figs. 4 and 5 compare the position of the leading edge of the cell population for assay 1 and assay 2 with the corresponding predictions from Eq. (4) using the appropriate parameter values given in Table 1. The solution of Eq. (4) is represented in terms of the $c(r,t)=0.019$ contour (Supplementary material). Overall, the agreement between the experiments and the model predictions indicates that the parameter estimates appear to accurately capture the observed differences between the two geometries, both with and without proliferation, and at all time points considered.

Results in Fig. 6 compare the time evolution of the observed values of $M(t)$ (Eq. (7)) with the corresponding predicted values of $M(t)$ using appropriately parameterised solutions of Eq. (4). We note that the prediction of the mathematical model at $t=24$ h for assay 2 appears to systematically underestimate $M(t)$. This small discrepancy could be due to our experimental procedure since the imaging process requires a brief interruption to the incubation conditions when the assay was stopped for imaging. We anticipate that this disruption would have a negligible impact on those experiments conducted for a long period of time whereas the impact could be more important for experiments conducted over a shorter period of time. Despite this discrepancy at one time point in assay 2, our overall comparison between the observations and the modelling predictions indicates that the parameterised model accurately predicts the time-evolution of the position of the leading edge and reliably captures the differences in our experiments where cell proliferation was either suppressed or permitted.

4.3.2. Cell density profiles

We now consider comparing the observed cell density profile with the cell density profile predicted by our parameterised mathematical model. Individual-scale images across a transect through the spreading population were used to estimate spatial distribution of the nondimensional cell density. We divided each transect into 20–30 subregions, each of length approximately 150 μm, along the transect axis. Fig. 7(a) and (f) shows the location of the transects relative to the entire population. Snapshots of the

Table 1
Summary of parameter estimates for assay 1 and assay 2 geometries with the uncertainty given in the parentheses.

Assay	Initial density	Diffusivity D (μm^2/h)	Proliferation rate λ (/h)	Doubling time $t_d=\ln(2)/\lambda$ (h)
1	Low	1700 (1000–1900)	0.056 (0.048–0.065)	12.4 (10.6–14.5)
	High	2900 (2400–3200)	0.059 (0.055–0.078)	11.7 (8.8–12.6)
2	Low	800 (500–1200)	0.042 (0.037–0.054)	16.5 (12.8–18.7)
	High	1500 (1000–1900)	0.041 (0.035–0.055)	16.9 (12.6–19.8)

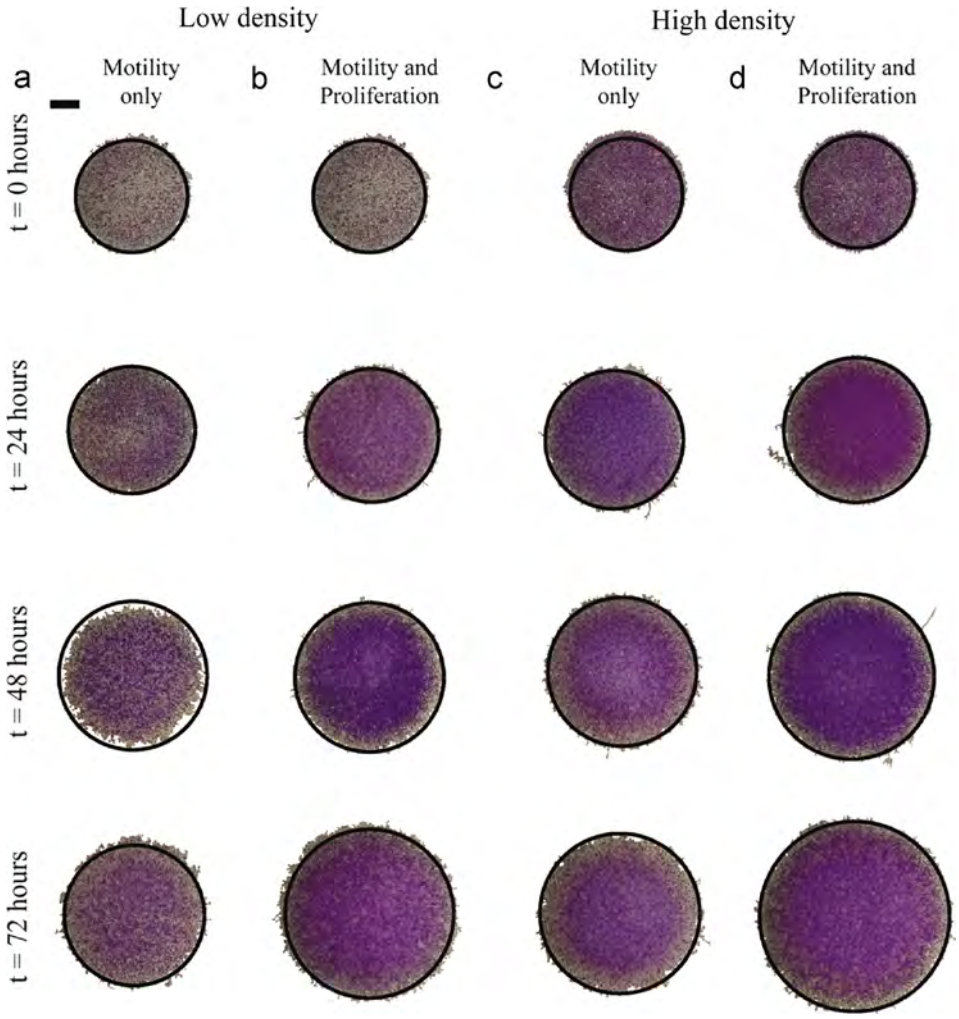

Fig. 4. Extent of spatial spreading in assay 1 is compared to the corresponding predictions of the mathematical model. The position of the leading edge of the spreading cell population in assay 1 was determined by analysing images from the experiments initialised with low cell density in (a) and (b), and high cell density in (c) and (d). Images in rows 1, 2, 3 and 4 show the spreading cell population at $t=0$, 24, 48 and 72 h, respectively. The coloured area corresponds to the spreading cell population. Experiments with Mitomycin-C pretreatment (motility only) are shown in the first and third columns, while experiments without Mitomycin-C pretreatment (motility and proliferation) are shown in the second and fourth columns. In each image, we superimpose the $c(r,t)=0.019$ contour of the relevant solution of Eq. (4) in black. The scale bar corresponds to 1500 μm. (For interpretation of the references to colour in this figure caption, the reader is referred to the web version of this paper.)

images analysed from experiments with a high initial cell density are given in Fig. 7(b)–(e) for assay 1, and in Fig. 7(g)–(j) for assay 2. Image analysis software was used to count the number of cells in each subregion, and this was converted into an estimate of the nondimensional cell density, $c(t)=\overline{c}(t)/K$, which was used to construct the histograms in Fig. 8. The appropriately parameterised solutions of Eq. (4) are superimposed onto these histograms. Comparing the solutions of Eq. (4) with the experimental measurements confirms that the appropriately parameterised model reliably captures the entire cell density profiles in assay 1 and assay 2, and for both types of experiments where cell proliferation was suppressed or not.

4.4. Comparing estimates of D and λ in different geometries

We now compare whether estimates of D and λ obtained by calibrating the model in one particular geometry can be used to predict the extent of spatial spreading in a different geometry. Results in Fig. 9 compare the population-scale images at $t=72$ h with the corresponding predictions of the mathematical model using both the estimates of D and λ obtained from assay 1 and the estimates of D and λ from assay 2. In all cases we see that the prediction of the mathematical model, parameterised with the appropriate estimates of D and λ, provides an excellent match to the observed spreading, as expected. However, we also show that the prediction of the mathematical model, parameterised with the alternative estimates of D and λ, provide a very poor prediction. The difference between the observed position of the leading edge and the prediction of the mathematical model is most evident in the proliferative populations where the discrepancy is as much as 500 μm. These comparisons confirm that estimates of D and λ obtained by focusing on one particular geometry may not be suitable to make predictions in another geometry.

Results in Fig. 10 present a similar comparison between the observed shape of the cell density profile near the leading edge and the predictions of the mathematical model. Cell density profiles within a distance of 2000 μm of the leading edge were constructed by dividing this region into 9–15 equidistant subregions of length approximately 100 μm. Image analysis software was used to count the number of cells in each subregion, and this count was converted into a nondimensional cell density, $c(t)=\overline{c}(t)/K$. Again, our results confirm that the predictions of the mathematical model, parameterised with the appropriate estimates of D and λ, provide a good match to the shape and position of the observed density profiles. In contrast, the prediction of the mathematical model, parameterised with the

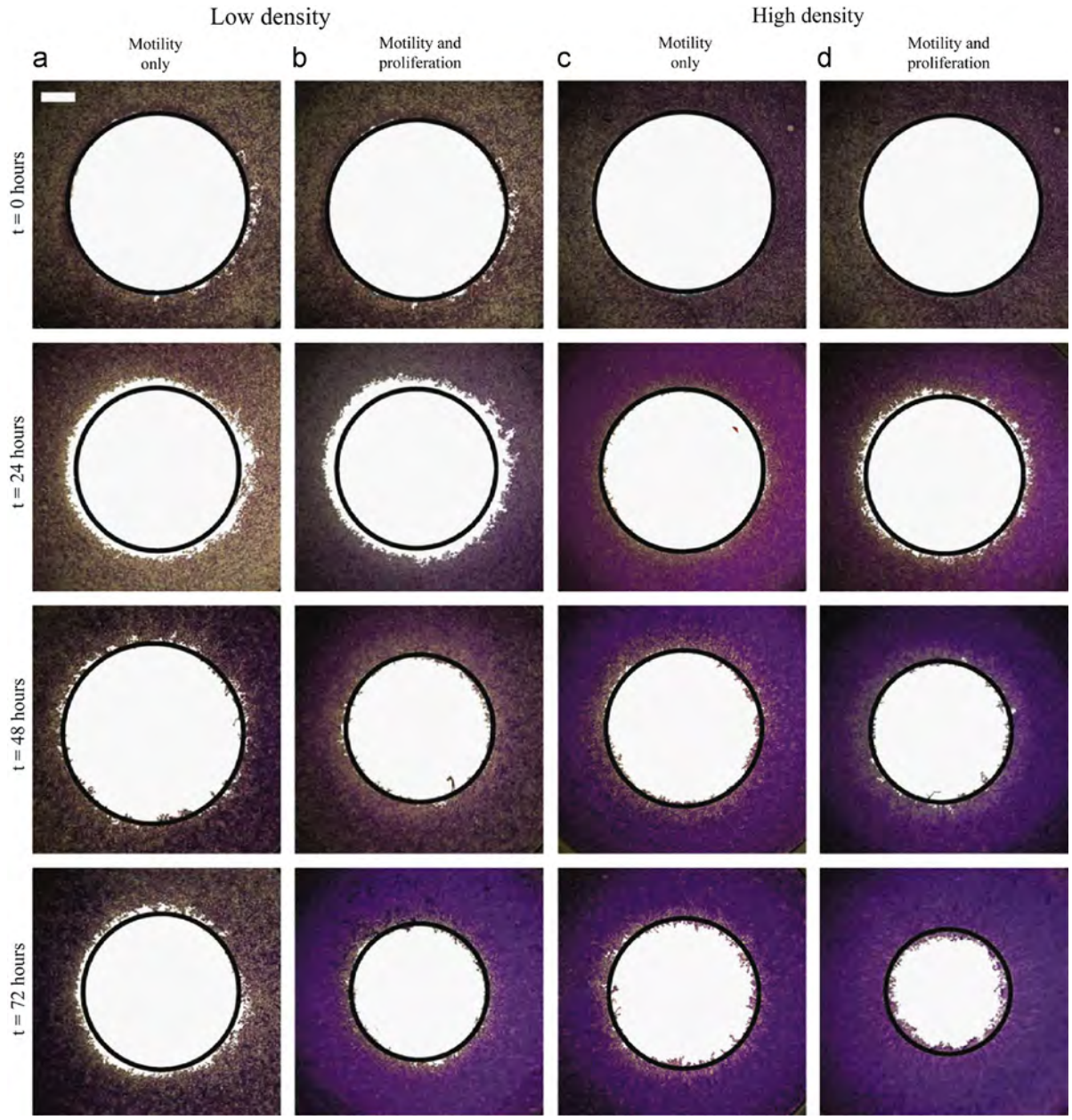

Fig. 5. Extent of spatial spreading in assay 2 is compared to the corresponding predictions of the mathematical model. The position of the leading edge of spreading cell population in assay 2 was determined by analysing images from the experiments initialised with low cell density in (a) and (b), and high cell density in (c) and (d). Images in rows 1, 2, 3 and 4 show the spreading cell population at $t=0$, 24, 48 and 72 h, respectively. The white circular area corresponds to the void region. Experiments with Mitomycin-C pretreatment (motility only) are shown in the first and third columns, while experiments without Mitomycin-C pretreatment (motility and proliferation) are shown in the second and fourth columns. In each image, we superimpose the $c(r,t)=0.019$ contour of the relevant solution of Eq. (4) in red. The scale bar corresponds to 1500 μm. (For interpretation of the references to colour in this figure caption, the reader is referred to the web version of this paper.)

alternative estimates of D and λ, fails to match either the position or the shape of the leading edge. Therefore, our results suggest that great care should be taken when estimating D and λ in one situation and then applying the parameterised model to make predictions in another situation.

Our data describing the shape of the cell density profile in Fig. 10 can also be used to provide a separate estimate of D by matching the solution of Eq. (4) with this data for the experiments where proliferation was suppressed. Additional results (Supplementary material) confirm that estimates of D obtained using this approach are very similar to our results reported in Section 4.1 where we focused on the leading edge data only. Most importantly, when we estimate D using the shape of the cell density profiles we find a very similar discrepancy between our estimates of D when we use the density profiles from assay 1 compared to the density profiles from assay 2. Although we have estimated D using both the density profiles and the leading edge data separately, we chose to focus on the results associated with the leading edge data since this method is simpler to implement since it avoids the need for counting individual cells and constructing cell density profiles.

5. Discussion and conclusion

Various approaches that attempt to investigate how populations of cells spread typically neglect the influence of the assay geometry (Kilian et al., 2010; Doxzen et al., 2013). In this work, we

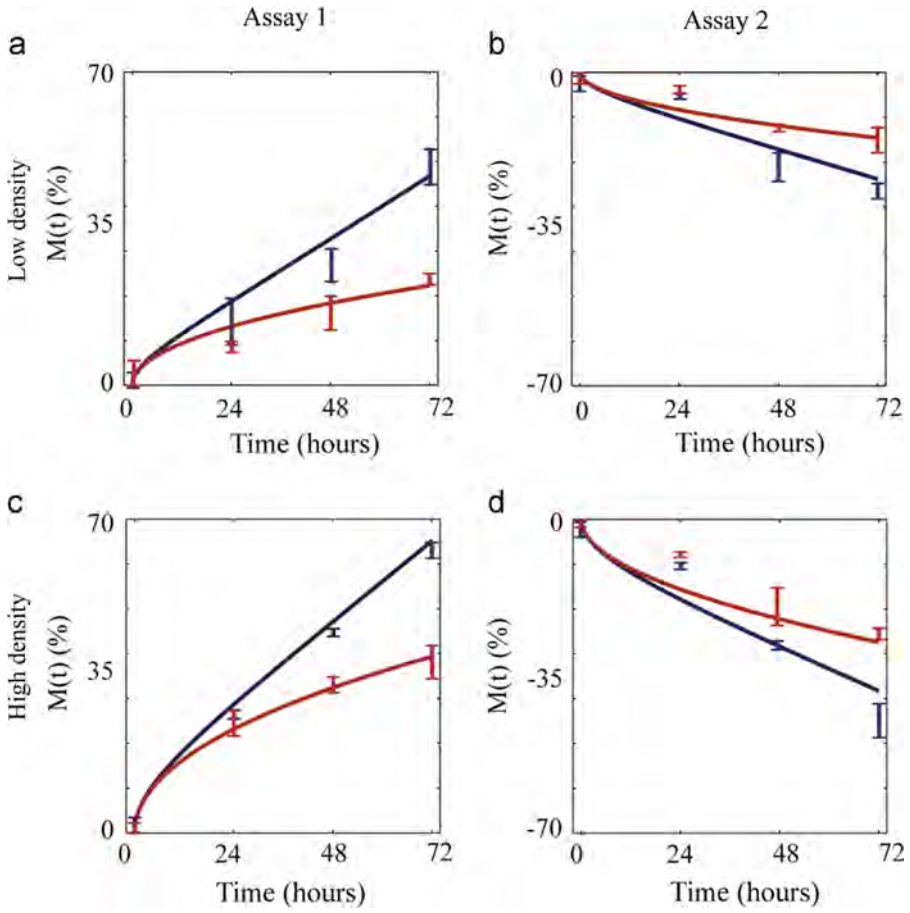

Fig. 6. Experimental measurements of the position of the leading edge of the spreading population were compared to the corresponding predictions of the mathematical model in terms of $M(t)$. The mean radii estimated from experimental images at $t=0$, 24, 48 and 72 h ($n=3$) were converted into a measurement of $M(t)$ using Eq. (7). The errors bars indicate one standard deviation from the mean. Results are given for both assay 1 and assay 2 for low (a) and (b), and high (c) and (d) initial cell densities, respectively. Solid curves represent $M(t)$ calculated using the position of the $c(r,t)=0.019$ contour from the relevant solution of Eq. (4). Red curves correspond to experiments with Mitomycin-C pretreatment, whereas blue curves correspond to experiments without Mitomycin-C pretreatment.

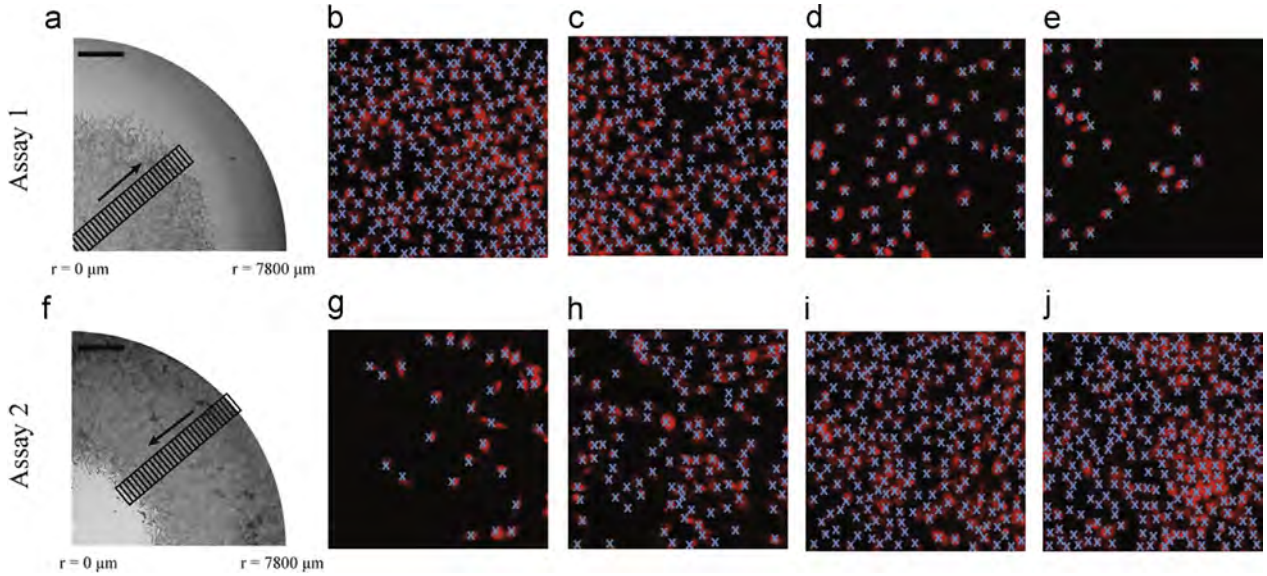

Fig. 7. Location of the subregions used to construct cell density profiles and individual-scale images showing the locations of cells within these subregions. Experimental cell density profiles were constructed by counting the number of cells in 20–40 subregions along a transect spanning the spreading cell population. The relative size and approximate location of these subregions are illustrated in (a) and (f), where the scale bar corresponds to 1500 μm. Individual-scale images in (b)–(e) and (g)–(j) show snapshots of various subregions of dimensions 250 μm × 250 μm. The subregions in (b)–(e) correspond to assay 1, and the value of the radial coordinate r in each of these subregions increases such that (b) is close to the centre of the well and (e) is located towards the edge of the outward spreading population. The subregions in (g)–(j) correspond to assay 2, and the value of the radial coordinate r in each of these subregions increases such that (g) is located close to the leading edge of the inward spreading population and (j) is located towards the edge of the well. The Propidium Iodide staining highlights the cell nucleus and blue crosses indicate cells that were counted in the analysis. (For interpretation of the references to colour in this figure caption, the reader is referred to the web version of this paper.)

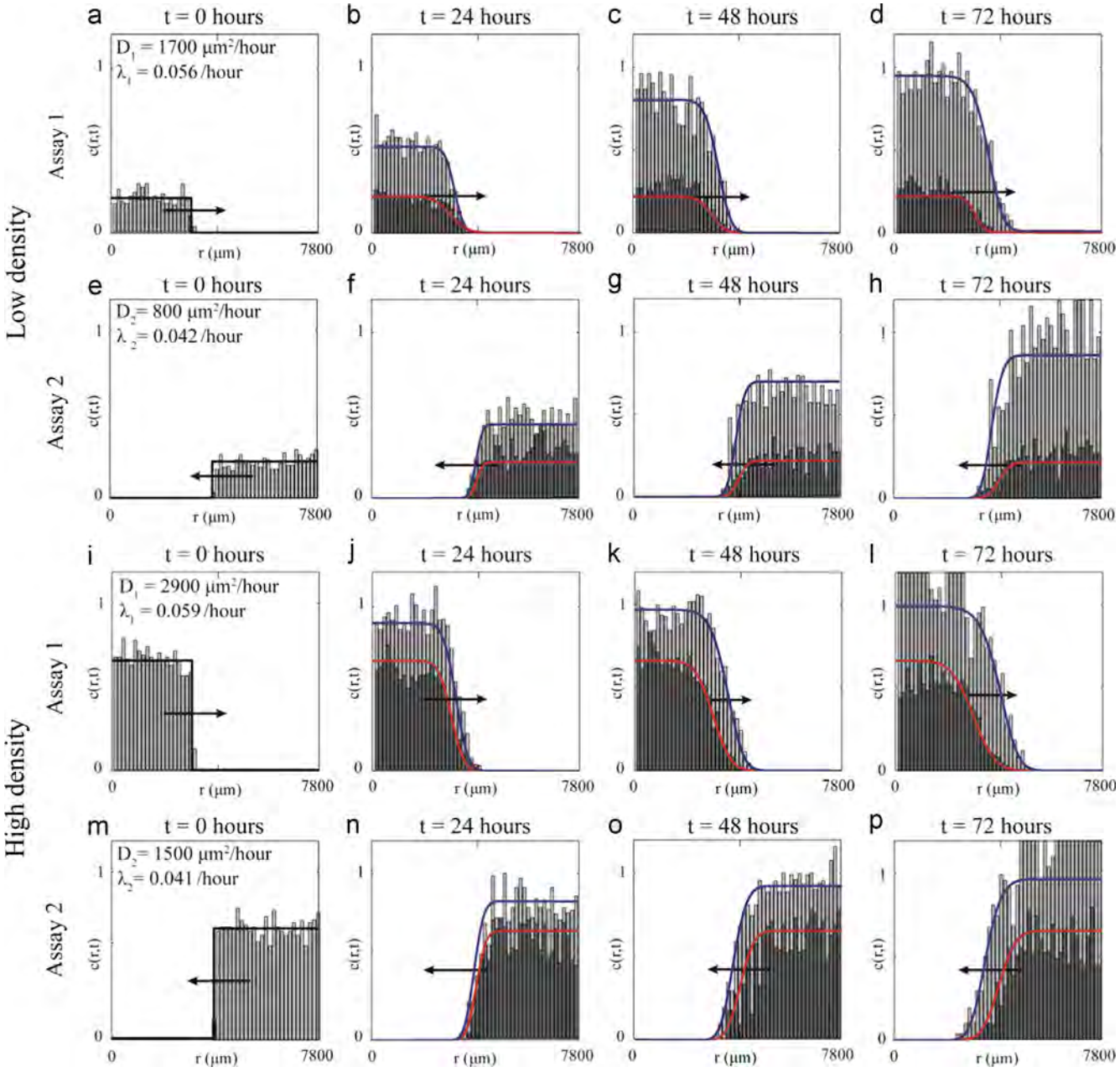

Fig. 8. Cell density profiles comparing the extracted experimental data and the relevant solution of Eq. (4) using the parameter estimates in Table 1. Assay 1 results for experiments both with (dark grey) and without Mitomycin-C (light grey) pretreatment, at $t=0$, 24, 48 and 72 h, are shown in rows 1 (low initial density) and 3 (high initial density). Equivalent results for assay 2 are shown in rows 2 (low initial density) and 4 (high initial density). Arrows indicate the direction of the spreading cell population. The red (motility only) and blue (motility and proliferation) curves superimposed on all results correspond to the relevant solutions of Eq. (4). (For interpretation of the references to colour in this figure caption, the reader is referred to the web version of this paper.)

used a circular barrier assay to analyse the spreading behaviour of a fibroblast cell population in two distinct geometries: (i) assay 1 resembled a tumour-like outward spreading process, and (ii) assay 2 resembled a wound-like inward spreading process. To quantify the differences between these assays we used a combined experimental and a mathematical modelling approach to estimate D from experiments where cell proliferation was suppressed. We then separately estimated λ from experiments where proliferation was not suppressed. Given our estimates of D and λ, we then independently verified that our parameterised model could predict both the position of the leading edge and the shape of the cell density profiles in both assays for two different initial densities.

Our results suggest that assay geometry can affect the behaviour of spreading cell populations since our estimate of D for assay 2 was up to 50% lower than our estimate of D for assay 1, while our estimate of λ was up to 30% lower for assay 2 compared to assay 1. This observation is important because most experimental and mathematical modelling studies of *in vitro* cell spreading typically focus on one geometry only and make the implicit assumption that observations and measurements in one geometry are relevant for others. Our results, highlighted in Figs. 9 and 10, indicate that this implicit assumption can produce misleading results.

This work highlights the importance of using mathematical modelling tools to quantify the contributions of cell motility and cell proliferation in driving the observed spreading behaviour. For example, standard measures of cell spreading, such as Eq. (7), do not provide any detailed information regarding how the

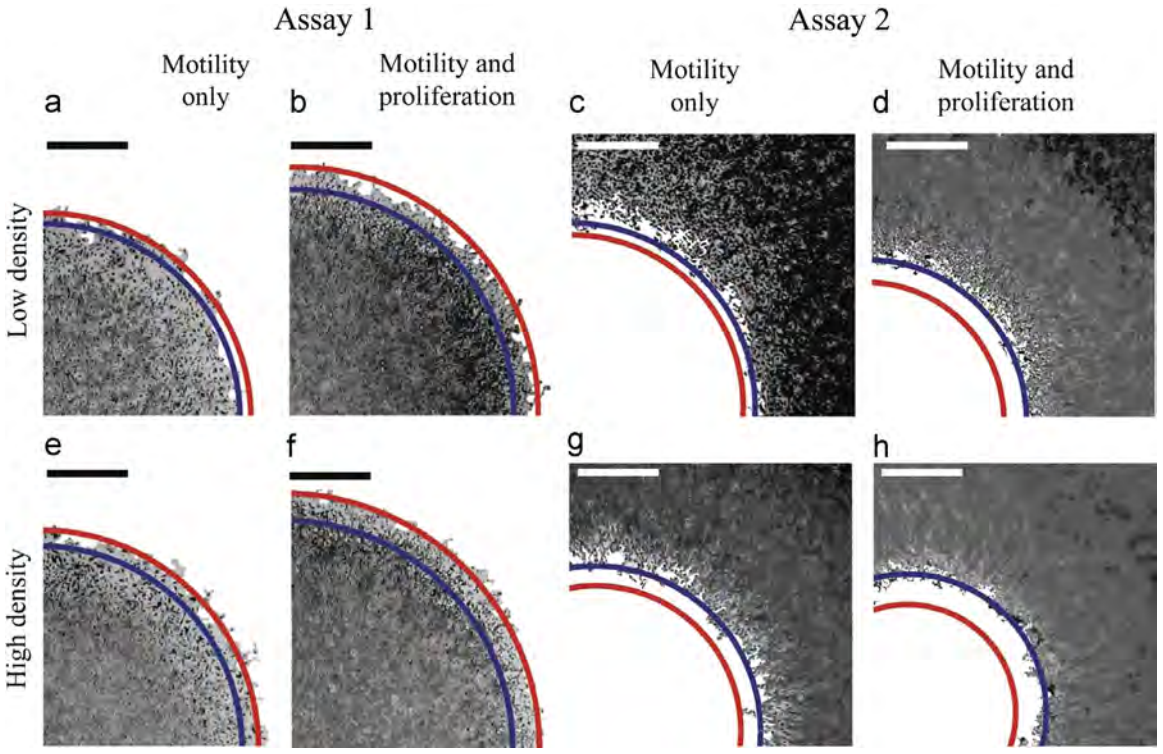

Fig. 9. Predicting the spread of a cell population using estimates of D and λ from a different geometry: comparing the location of the leading edge. Population-scale images that correspond to experiments at $t=72$ h are given in (a)–(d) for a low initial cell density, and in (e)–(h) for a high initial cell density. Experiments with Mitomycin-C pretreatment (motility only) are shown in the first and third columns, while experiments without Mitomycin-C pretreatment (motility and proliferation) are shown in the second and fourth columns. In each image we superimpose the $c(r,t)=0.019$ contour of the relevant solution of Eq. (4) using the parameter estimates for assay 1 (red) and for assay 2 (blue). The scale bar corresponds to 1500 μm. (For interpretation of the references to colour in this figure caption, the reader is referred to the web version of this paper.)

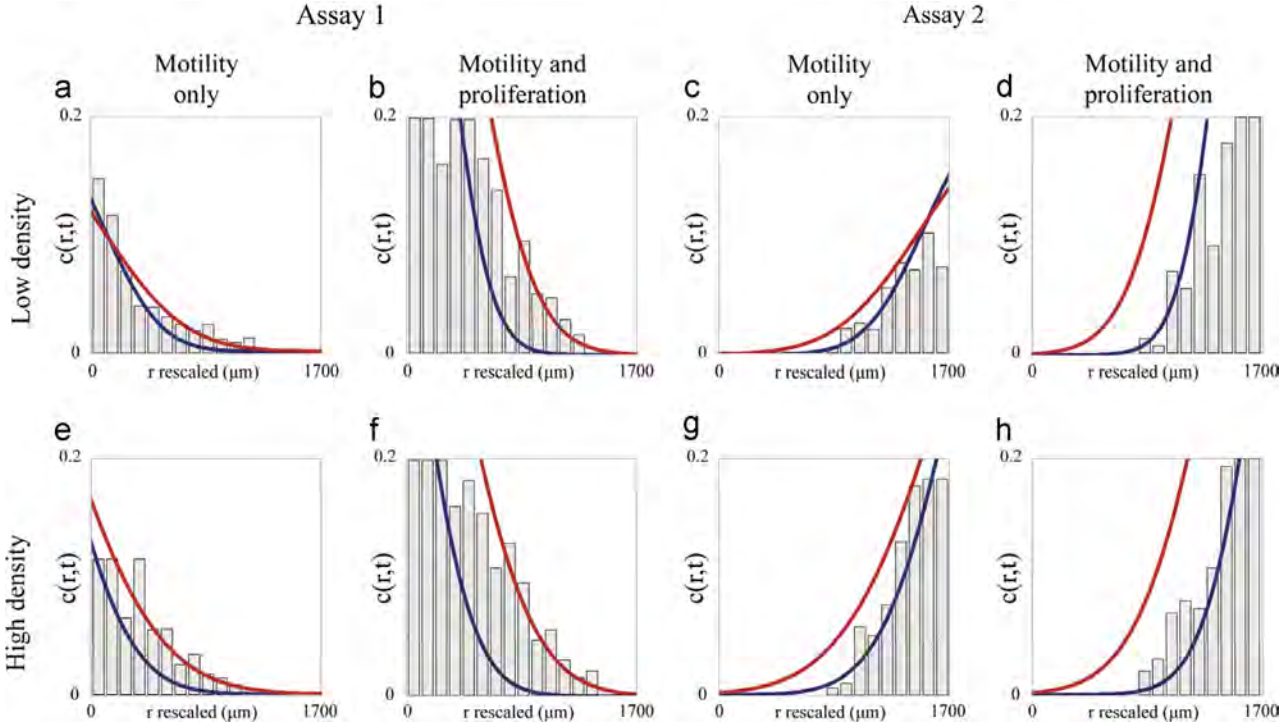

Fig. 10. Predicting the spread of a cell population using estimates of D and λ from a different geometry: comparing the cell density profile at the leading edge of the spreading population. Cell density profiles that correspond to experiments at $t=72$ h are given in (a)–(d) for a low initial cell density, and in (e)–(h) for a high initial cell density. Experiments with Mitomycin-C pretreatment (motility only) are shown in the first and third columns, while experiments without Mitomycin-C pretreatment (motility and proliferation) are shown in the second and fourth columns. In each image, we superimpose the solution of Eq. (4) using the parameter estimates for assay 1 (red) and for assay 2 (blue). (For interpretation of the references to colour in this figure caption, the reader is referred to the web version of this paper.)

underlying mechanisms contribute to the observed spreading. Furthermore we have shown that these standard measures cannot be compared between different geometries since comparing estimates of $M(t)$ for assay 1 with estimates of $M(t)$ for assay 2 is not insightful. Our analysis of the data using Eq. (7) could have been performed in terms of the observed area, $A(t)$, instead of the observed radius, $R(t)$ (Ashby and Zijlstra, 2012; McKenzie et al., 2011; Zaritsky et al., 2011; Treloar and Simpson, 2013). However, regardless of whether $M(t)$ is measured in terms of $R(t)$ or $A(t)$ we find the same trends in the data which means that our conclusions about $M(t)$ are relevant regardless of these details. In contrast, a mathematical modelling approach that explicitly represents the underlying cell motility and cell proliferation mechanisms can overcome this difficulty since we can extract, and quantify, detailed information about both the cell motility and cell proliferation mechanisms separately.

The focus of our work has been to assess quantitative differences between two different assay geometries. It is also worthwhile to discuss some qualitative differences between assay 1 and assay 2. We found that the experimental procedure for assay 1 was more straightforward to implement and analyse for two reasons. First, assay 2 requires the use of a greater number of cells in the experimental procedure which means that discrete simulations are more time consuming to perform. Second, we found that it is more difficult to initialise the cells uniformly outside the barrier compared to inside the barrier. Despite this difficulty, we always ensured that all experiments were initiated as uniformly as possible by performing a large number of experiments and discarding all those results in which the cells were not uniformly initialised.

To illustrate the consequences of our study, we confirmed that estimates of D and λ from one particular geometry could give misleading results by applying the mathematical model parameterised with these estimates to make a prediction of the cell spreading in the other geometry that we considered. These results confirmed that the solution of our mathematical model with estimates of D and λ from assay 1 failed to predict the position of the leading edge and the shape of the density profile in assay 2. Similarly, we confirmed that the solution of the mathematical model with estimates of D and λ from assay 2 failed to predict the position of the leading edge and the shape of the density profile in assay 1.

A key assumption in this work is that the cell spreading always took place in a two-dimensional monolayer for the entire duration of the experiments. Initially, we also performed experiments where cells were placed into and around the barriers at a higher density than we reported here. In these additional experiments we observed that cells did not form a monolayer due to the high initial density. These additional experiments were not analysed here since the two-dimensional model is inappropriate.

One limitation of our study is that we have not resolved the question of why cells appear to behave differently in different geometries. One possible mechanism that could explain our observations is that the total number of cells initially present in assay 2 is always larger than that in assay 1. Assuming that each cell consumes nutrients at a particular rate, we might expect that the supply of nutrients in assay 2 would be depleted faster than that in assay 1 which is consistent with our observations that D and λ are apparently smaller in assay 2. To test this hypothesis we suggest that additional measurements of the availability of nutrients could be made and that these measurements could be incorporated into an extension of the mathematical model where D and λ explicitly depend on nutrient availability. This suggestion could be important since many mathematical models of collective cell spreading make the implicit assumption that the supply of nutrients is unlimited (Maini et al. 2004a,b; Sengers et al., 2007; Cai et al., 2007). Other options for extending this work are to include further experiments to examine the role of other geometries, such as using barriers with different curvatures. Unfortunately the barriers that we used in this study are fixed in shape and so a different experimental apparatus would be required to study such an extension.

Acknowledgements

We acknowledge the Australian Research Council (DP120100551) and the Royal Society International Exchange Scheme. We appreciate support from Parvathi Haridas, Kerry Manton and David Leavesley, as well as the comments from two anonymous referees.

Appendix A. Supplementary material

Supplementary data associated with this paper can be found in the online version at http://dx.doi.org/10.1016/j.jtbi.2014.04.026.

References

Anderson, A.R.A., Chaplain, M.A.J., 1998. Continuous and discrete mathematical models of tumor-induced angiogenesis. Bull. Math. Biol. 14, 576–594.
Anderson, A.R.A., Chaplain, M.A.J., Rejniak, K.A., 2007. Single-cell-based models in biology and medicine. Birkhauser, Basel.
Ashby, W.J., Zijlstra, A., 2012. Established and novel methods of interrogating two-dimensional cell migration. Integr. Biol. 4, 1338–1350.
Aubert, M., Fereol, S., Christov, C., Grammaticos, B., 2006. A cellular automaton model for the migration of glioma cells. Phys. Biol. 3, 93–100.
Bradie, B., 2005. A Friendly Introduction to Numerical Analysis, 1st Edition Pearson Higher Education, USA.
Brock, A., Chang, E., Ho, C., LeDuc, P., Jiang, X., Whitesides, G., Ingber, D., 2003. Geometric determinants of directional cell motility revealed using microcontact printing. Langmuir 19, 1611–1617.
Cai, A.Q., Landman, K.A., Hughes, B.A., 2007. Multi-scale modeling of a wound-healing cell migration assay. J. Theor. Biol. 245, 576–594.
Chang, H., Sneddon, J., Alizadeh, A., Sood, R., West, R., Montogomery, K., Chi, J., van de Rijn, M., Botstein, D., Brown, P., 2004. Gene expression signature of fibroblast serum response predicts human cancer progression: similarities between tumors and wounds. PLoS Biol. 2, 0206–0214.
Chowdhury, D., Schadschneider, A., Nishinari, K., 2005. Physics of transport and traffic phenomena in biology: from molecular motors and cells to organisms. Phys. Life Rev. 2, 318–652.
Clark, R., 1996. The Molecular and Cellular Biology of Wound Repair, 1st Edition Plenium, New York.
Codling, E.A., Plank, M.J., Benhamou, S., 2008. Random walks models in biology. J. R. Soc. Interface 5, 813–834.
Coussens, L., Werb, Z., 2002. Inflammation and cancer. Nature 420, 860–867.
Decaestecker, C., Debeir, O., Van Ham, P., Kiss, R., 2007. Can anti-migratory drugs be screened in vitro? a review of 2D and 3D assays for the quantitative analysis of cell migration. Med. Res. Rev. 27, 149–176.
Deroulers, C., Aubert, M., Badoual, M., Grammaticos, B., 2009. Modeling tumor cell migration: from microscopic to macroscopic models. Phys. Rev. E 79, 031917.
Doxzen, K., Vedula, S., Leong, M., Hirata, H., Gov, N., Kabla, A., Ladoux, B., Lim, C., 2013. Guidance of collective cell migration by substrate geometry. Integr. Biol. 5, 1026–1035.
Friedl, P., Gilmour, D., 2009. Collective cell migration in morphogenesis, regeneration and cancer. Nat. Rev. Mol. Cell Biol. 10, 445–457.
Geho, D., Bandle, R., Clair, T., Liotta, L., 2005. Physiological mechanisms of tumor cell invasion and migration. Physiology 20, 194–200.
Gough, W., Hulkower, K., Lynch, R., Mcglynn, P., Uhlik, M., Yan, L., Lee, J., 2011. A quantitative, facile, and high-throughput image-based cell migration methods is a robust alternative to the scratch assay. J. Biomol. Screen., 155–163.
ImageJ, ImageJ User Guide: Research Services Branch, National Institute of Health. ⟨http://rsbweb.nih.gov/ij/docs/guide/146-29.html⟩ (accessed on November 2013).
Kam, Y., Guess, C., Estrada, L., Weidow, B., Quaranta, V., 2008. A novel circular invasion assay mimics in vivo invasive behavior of cancer cell lines and distinguishes single-cell motility in vitro. BMC Cancer 8, 198–210.
Kam, Y., Karperien, A., Weidow, B., Estrada, L., Anderson, A.R., Quaranta, V., 2009. Nest expansion assay: a cancer systems biology approach to *in vitro* invasion measurements. BMC Res. Notes 2, 130–139.
Kilian, K., Bugarija, B., Lahn, B., Mrksich, M., 2010. Geometric cues for directing the differentiation of mesenchymal stem cells. Proc. Natl. Acad. Sci. 107, 4872–4877.

Kramer, N., Walzl, A., Unger, C., Rosner, M., Krupitza, G., Hengstschlager, M., Dolznig, H., 2013. *in vitro* cell migration and invasion assays. Mutat. Res. 752, 10–24.
Lutolf, M., Hubbell, J., 2005. Synthetic biomaterials as instructive extracellular microenvironments for morphogenesis in tissue engineering. Nat. Biotechnol. 23, 47–55.
Maini, P.K., McElwain, D.L.S., Leavesley, D.I., 2004a. Traveling wave model to interpret a wound-healing cell migration assay for human peritoneal mesothelial cells. Tissue Eng. 10, 475–482.
Maini, P.K., McElwain, D.L.S., Leavesley, D.I., 2004b. Traveling waves in a wound healing assay. Appl. Math. Lett. 17, 575–580.
Martin, P., 1997. Wound-healing—aiming for perfect skin regeneration. Science 276, 75–81.
MATLAB, Image Acquisition Toolbox User Guide r2012b: Mathworks. URL: ⟨http://www.mathworks.com.au/products/image/⟩ (accessed on March 2014).
McDougall, S.R., Watson, M.G., Devlin, A.H., Mitchell, C.A., Chaplain, M.A.J., 2012. A hybrid discrete-continuum mathematical model of pattern prediction in the developing retinal vasculature. Bull. Math. Biol. 74, 2272–2314.
McKenzie, A.J., Campbell, S.L., Howe, A.K., 2011. Protein kinase a activity and anchoring are required for ovarian cancer cell migration and invasion. PLoS One 6, e26552.
Murray, J.D., 2002. Mathematical Biology I: An Introduction, 3rd Edition Springer-Verlag, Heidelberg.
Plank, M.J., Simpson, M.J., 2013. Lattice-free models of cell invasion: discrete simulations and travelling waves. Bull. Math. Biol. 75, 2150–2166.
Sadeghi, M.H., Seitz, B., Hayashi, S., LaBree, L., McDonnell, P.J., 1998. in vitro effects of Mitomycin-c on human keratocytes. J. Refract. Surg. 14, 534–540.
Schafer, M., Werner, S., 2008. Cancer as an overhealing wound: an old hypothesis revisited. Nat. Rev. Mol. Cell Biol. 10, 445–457.
Sengers, B.G., Please, C.P., Oreffo, R.O.C., 2007. Experimental characterization and computational modelling of two-dimensional cell spreading for skeletal regeneration. J. R. Soc. Interface 4, 1107–1117.
Sherratt, J.A., Murray, J.D., 1990. Models of epidermal wound healing. Proc. R. Soc. Lond. B 241, 29–36.
Simpson, M.J., Landman, K.A., Clement, T.P., 2005. Assessment of a non-traditional operator split algorithm for simulation of reactive transport. Math. Comput. Simulat. 70, 44–60.
Simpson, M.J., Landman, K.A., Hughes, B.D., 2010. Cell invasion with proliferation mechanisms motivated by time-lapse data. Physica A 389, 3779–3790.
Simpson, M.J., Treloar, K.K., Binder, B.J., Haridas, P., Manton, K.J., Leavesley, D.I., McElwain, D.L.S., Baker, R.E., 2013. Quantifying the roles of cell motility and cell proliferation in a circular barrier assay. J. R. Soc. Interface 10, 20130007.
Swanson, K.R., Bridge, C., Murray, J.D., Alvord, E.C., 2003. Virtual and real brain tumors: using mathematical modeling to quantify glioma growth and invasion. J. Neurol. Sci. 216, 1–10.
Treloar, K.K., Simpson, M.J., 2013. Sensitivity of edge detection methods for quantifying cell migration assays. PLoS One 8, e67389.
Treloar, K.K., Simpson, M.J., Haridas, P., Manton, K.J., Leavesley, D.I., McElwain, D.L.S., Baker, R.E., 2013. Multiple types of data are required to identify the mechanisms influencing the spatial expansion of melanoma cell colonies. BMC Syst. Biol. 7, 137.
Turner, S., Sherratt, J.A., 2002. Intracellular adhesion and cancer invasion: a discrete simulation using the extended Potts model. J. Theor. Biol. 216, 85–100.
Turner, S., Sherratt, J.A., Painter, K.A., Savill, N.J., 2004. From a discrete to a continuous model of biological cell movement. Phys. Rev. E 69, 021910.
Valster, A., Tran, N., Nakada, M., Berens, M., Chan, A., Symons, M., 2005. Cell migration and invasion assays. Methods 37, 208–215.
Van Horssen, R., Ten Hagen, T.L.M., 2010. Crossing barriers: the new dimension of 2D cell migration assays. J. Cell Physiol. 226, 288–290.
Vedula, S.R.K., Leong, M.C., Lai, T.L., Hersen, P., Kabla, A.J., Lim, C.T., Ladoux, B., 2012. Emerging modes of collective cell migration induced by geometrical constraints. Proc. Natl. Acad. Sci. 109, 12974–12979.
Vogel, V., Sheetz, M., 2006. Local force and geometry sensing regulate cell functions. Nat. Rev. Mol. Cell Biol. 7, 265–275.
Weinberg, R.A., 2006. The Biology of Cancer. Garland Publishing, USA.
Woodhouse, E., Chuaqui, R., Liotta, L., 1997. General mechanisms of metastasis. Cancer 80, 1529–1537.
Zaritsky, A., Natan, S., Horev, J., Hecht, I., Wold, L., Ben-Jacob, E., Tsarfaty, I., 2011. Cell motility dynamics: a novel segmentation algorithm to quantify multi-cellular bright field microscopy images. PLoS One 6, e27593.
Zaritsky, A., Manor, N., Wolf, L., Ben-Jacob, E., Tsarfaty, I., 2013. Benchmark for multi-cellular segmentation of bright field microscopy images. BMC Bioinform. 14, 319–324.